Chemical Engineering Journal 429 (2022) 132244

Contents lists available at ScienceDirect

Chemical Engineering Journal

journal homepage: www.elsevier.com/locate/cej

The Calcium Looping process for energy storage: Insights from *in situ* XRD analysis

Santiago Medina-Carrasco [a,*], Jose Manuel Valverde [b,*]

[a] X-Ray Laboratory (CITIUS), Universidad de Sevilla, Avenida Reina Mercedes, 4B, 41012 Sevilla, Spain
[b] Facultad de Física, Universidad de Sevilla, Avenida Reina Mercedes s/n, 41012 Sevilla, Spain

ARTICLE INFO

Keywords:
CO_2 capture
Calcium looping
Limestone
Dolomite
Thermochemical energy storage
Concentrated solar power

ABSTRACT

This work reports a novel *in situ* XRD analysis on the multicycle calcination/carbonation of natural limestone and dolomite at relevant conditions for thermochemical energy storage (TCES) in concentrated solar power (CSP) plants. The experiments allow analysing noninvasively the time evolution of the different phases involved in the Calcium Looping (CaL) process. Our work has revealed new key features to understand the progressive loss of multicyclic carbonation reactivity of the CaO derived from calcination. The $CaCO_3$ structure formed in the first step of dolomite decomposition has smaller unit cell volume than the $CaCO_3$ naturally present in limestone. The CaO that stems from decomposition of the $CaCO_3$ derived from dolomite first decomposition shows a greater carbonation reactivity compared to the CaO derived from limestone. The smaller size of the CaO nascent crystals and their relatively higher reactivity for dolomite compared to limestone is related to the presence of inert MgO crystals, which prevent CaO sintering and crystallite growth. However, the size of the MgO crystals derived from dolomite decomposition increases monotonically with time, which progressively hampers their hindrance effect. Our work also shows a positive correlation between the growth of the CaO crystallite size and the decline of preferred orientation in the CaO (1 0 0) plane as the number of cycles is increased and CaO loses reactivity. The observed evolution with the cycles of CaO crystallite size and reactivity can be attributed to the incompletion of carbonation. The unreacted CaO that remains in the calcination step suffers severe sintering which hinders its reactivity. Thus, the fraction of fresh, reactive CaO derived from $CaCO_3$ decomposition that nucleates on the old and less reactive CaO declines progressively with the cycles.

1. Introduction

The calcium looping (CaL) process, which is based on the reversible calcination/carbonation reaction of $CaCO_3$/CaO at high temperature, has drawn a high interest in recent years for CO_2 capture in fossil fuel based power plants [1,2] and thermochemical energy storage (TCES) in concentrating solar plants (CSP) [3–5]. Among the possible CaO precursors, natural limestone (near to 100% $CaCO_3$) is the most widely investigated, mainly due to its low cost (2014 US price of 10.42 $/ton) [6], abundance and low toxicity [7]. Dolomite ($CaMg(CO_3)_2$) is another natural precursor of great interest [8,9], with advantages similar to limestone and a cost on the same order (2014 US price of 12.90 $/ton) [10].

One of the top expanding renewable energy technologies nowadays is CSP [5] as it enables large-scale electricity generation under demand due to the possibility of energy storage in the form of heat at relatively low cost [4]. Thermochemical Energy Storage (TCES) is being investigated extensively in recent years [1,2]. Essentially, TCES is based on using heat from concentrated solar radiation, reaching temperatures near ~1000 °C in CSP with tower technology, to drive an endothermic chemical reaction. The reaction products are stored separately, so that they can be used to generate power under demand from the heat released in the reverse exothermic reaction [1,11,12]. TCES based on the CaL process has been the subject of large number of experimental works at laboratory scale [13–18], process simulations [5,8,19–21] and is being currently tested at the pilot scale [22]. A main advantage of the CaL process, which relies on the calcination/carbonation reaction of $CaCO_3$/CaO (1) [8,9]

$$CaCO_3 \rightleftarrows CaO + CO_2(g) \quad \Delta_r H_0 = +177.8\ kJ\ mol^{-1} \tag{1}$$

is that the theoretical storage energy density (~3.2 GJ m^{-3}) is much higher than the energy density of molten salts currently used in

* Corresponding authors.
E-mail addresses: sanmedi@us.es (S. Medina-Carrasco), jmillan@us.es (J.M. Valverde).

https://doi.org/10.1016/j.cej.2021.132244
Received 22 June 2021; Received in revised form 11 August 2021; Accepted 31 August 2021
Available online 4 September 2021

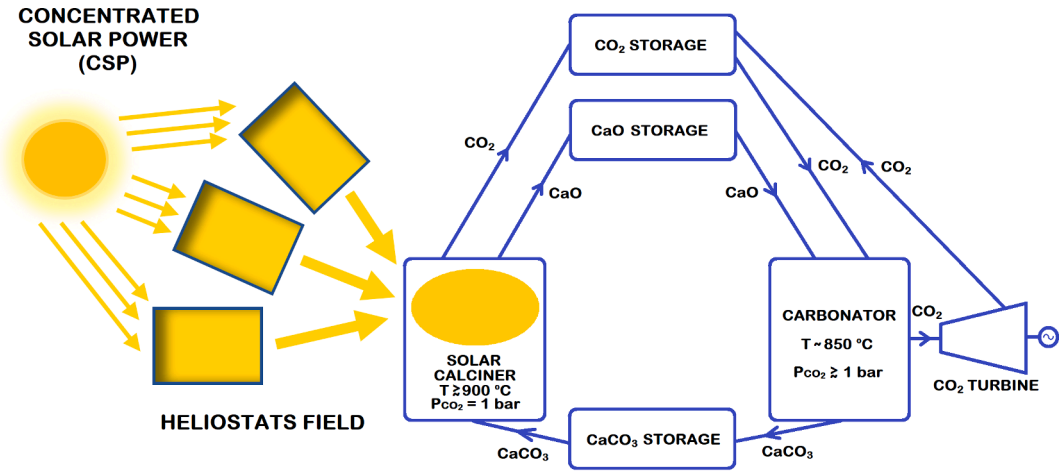

Fig. 1. Flow diagram of the Calcium-Looping thermochemical energy storage system for Concentrated Solar Power plants (adapted from [27]).

commercial CSP plants for sensible heat storage (~0.8 GJ m^{-3}). Moreover, the reaction products can be stored at ambient temperature without significant losses and, in contrast with molten salts, are not corrosive.

The CaL process has been studied in depth in the last decades for its application to capture CO_2 in fossil fuel based power plants, showing already good results in large scale pilot plants (1–2 MWt) [23,24]. The CaL process for CO_2 capture is based on the carbonation of CaO at temperatures of the order of 650 °C in a fluidized-bed carbonator, where the CaO particles are fluidized by the post combustion gas at an absolute pressure of 1 bar and with a low CO_2 concentration (~15 vol%). The carbonated particles are transported to a second fluidized bed calciner reactor, where they are subjected to temperatures above 900 °C in an atmosphere of high CO_2 concentration. The CO_2 released from the calciner is recovered and subjected to compression and storage. After calcination, the regenerated CaO particles are transported to the carbonator reactor for a new cycle [5].

The integrated CaL-CSP technology for TCES consists basically of a solar calciner, CaO and $CaCO_3$ storage tanks, a CO_2 compression storage system, a carbonator and a CO_2 turbine for energy generation [5]. The process for energy storage begins with the calcination of the $CaCO_3$ particles using concentrated solar energy to achieve the necessary heat for decomposition. CaO and CO_2, obtained as by-products of the reaction, are stored separately to be used under demand in a carbonator reactor. The heat released from the exothermic carbonation reaction is used to generate electricity through a gas turbine. The technical complexity of the integrated system is minimized by operating calcination, carbonation and power generation in a closed CO_2 circuit as schematized in Fig. 1 [5,25]. Calcination is carried out under pure CO_2 at atmospheric pressure at temperatures above 900 °C, which are achievable in CSP plants based on tower type technology [5]. On the other hand, carbonation under pure CO_2 can be performed at around 850 °C, which provides high temperature heat for efficient power generation [26]. Analysing the calcination/carbonation multicycle behaviour of natural CaO precursors, such as limestone or dolomite, in a CO_2 closed circuit is therefore of great interest for optimizing the CaL-CSP integration [25] at large scale.

A main objective of the CaL process is to achieve full calcination in the typically short residence times that the $CaCO_3$ solids remain in the calciner [5]. To accomplish this goal, an initially proposed method was to use He in the calciner atmosphere, since it accelerates calcination and lowers the calcination temperature below ~725 °C [28,29]. Calcination at this low temperature would reduce the loss of multicycle CaO activity predominantly caused by sintering in the calcination stage as inferred from TGA and ex situ SEM/XRD analysis [16,28]. Helium could be separated from the CO_2 released during calcination using state-of-the-art membrane technologies. Nonetheless, He/CO_2 separation would increase the complexity, energy penalty and cost of the technology [16,21]. Another possible technique investigated to accelerate $CaCO_3$ decomposition was the addition of humidity to the calciner [5,25]. However, this would imply including an intermediate condensation stage just after calcination in the CaL circuit, thus also increasing the complexity, technical feasibility, and energy cost of the process. Moreover, the presence of humidity at high concentrations in the calcining atmosphere has a significant effect on increasing the size of the crystallites promoting sintering of the resulting CaO, which can have negative consequences on its reactivity [25,30–34]. Thus, from the practical point of view, the use of a closed CO_2 circuit for calcination/carbonation and power generation stands nowadays as the most feasible technology to integrate the CaL process in CSP plants.

A main inconvenient though of the use of a closed CO_2 circuit for carbonation/calcination cycles at high temperatures is CaO deactivation. Thus, a better understanding of the mechanisms that govern this loss of activity is of great interest. The main reasons proposed for CaO reactivity decay are pore plugging [35] and sintering as derived from *ex-situ* SEM and XRD studies [36]. However, it is unclear how crystal size evolves along the cycles. Alternatively, ab initio simulations have suggested that a possible cause of the CaO loss of activity is the preferential growth with the number of cycles of determined CaO crystallographic planes where CO_2 adsorption is less favourable [37,38]. In other works, experimental evidence of a preferred crystallographic orientation between carbonate and oxide in the topotactic decomposition mechanism of calcite has been presented [39,40]. However, the theoretical mechanism suggested by ab-initio simulations has not been experimentally tested yet. To this end, *in-situ* XRD measurements would be necessary, which would allow crystallographic characterization of the phases involved during multiple calcination/carbonation cycles. The present study is aimed at this goal. This research has been carried out in the frame of the H2020 European project SOCRATCES [22], coordinated by the University of Seville, to demonstrate at the pilot scale the suitability of the CaL process to store energy in thermochemical form.

2. Experimental materials and methods

The results here presented have been obtained using aerodynamically classified natural limestone from KSL Staub Technik GmbH (Germany) and dolomite from Bueres quarry (Spain). To carry out the experiments, samples were sieved to limit their size below 45 μm in

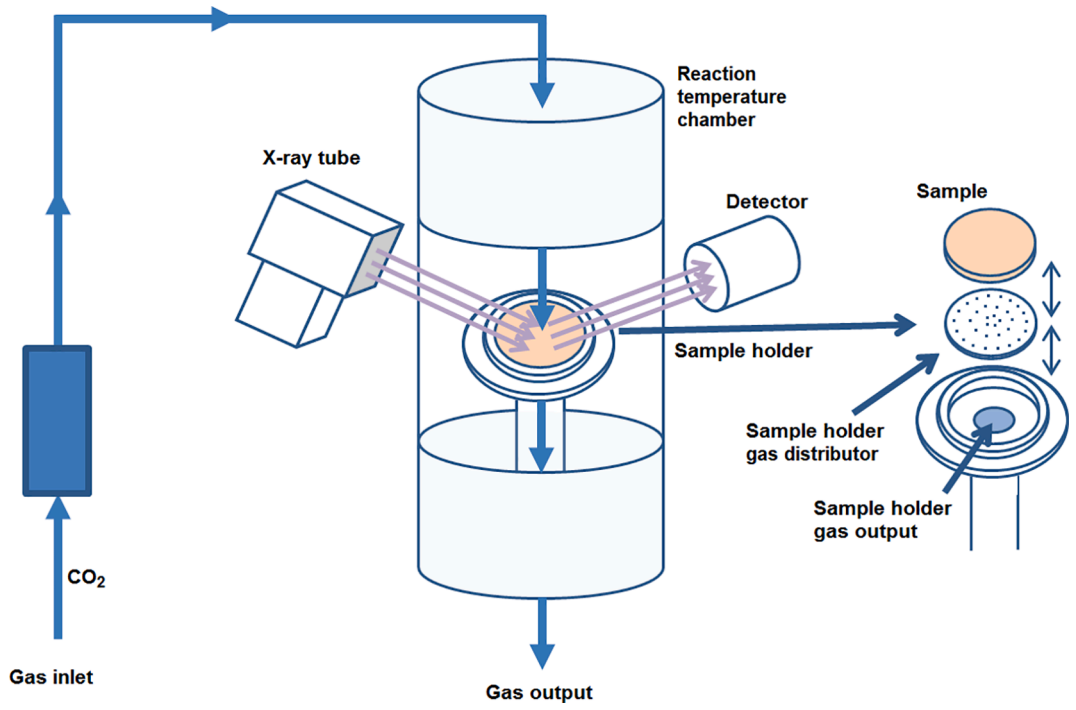

Fig. 2. Schematic view of the experimental setup used in this work for *in situ* XRD analysis of calcination/carbonation cycles.

order to minimize decrepitation during decomposition in the initial calcination stage [27,41,42], which would adversely affect *in situ* XRD characterization.

Calcination/carbonation experiments were carried out under atmospheric pressure in a continuous flow of 1000 cm^3/min pure CO_2. 10 °C/min temperature ramps were used for all experiments. Initially, the samples were preheated by increasing temperature from ambient to 850 °C. At this temperature two XRD diffractograms were registered. For calcination in the first cycle (Cycle 1) temperature was increased to 940 °C and a total of six XRD diffractograms were recorded to ensure full decarbonation. The temperature was then lowered to 850 °C for carbonation and two XRD diffractograms were acquired. A total of 10 calcination/carbonation cycles were carried out. These calcination/carbonation cycles are representative of conditions to be expected in the CaL process for TCES in CSP plants in a closed CO_2 circuit [5]. Reproducibility of the results was checked by repeating the experiments twice.

Figure 2 presents a schematization of the experimental setup used in the *in-situ* XRD experiments. A detailed description is available elsewhere [43].

XRD tests were performed by means of a Bruker (Germany) model D8 Advance powder diffractometer, featuring an Anton Paar (Austria) XRK900 reaction temperature chamber. The diffractometer is equipped with a high resolution VÅNTEC-1 position sensitive detector complemented by a radial Soller slits system. To avoid possible misalignments in the position or deformation of the sample due to the use of the temperature chamber, the diffractometer uses a parallel incident beam by means of large size sealed Göbel mirrors (60 mm) for CuKα radiation ($\lambda = 0.15405$ nm). Temperature control is accurately achieved by means of NiCr/NiAl thermocouples placed very close to the sample holder inside the temperature chamber. The powder diffractometer was calibrated according to the manufacturer's specifications. Corundum, LaB_6 and silicon standards were tested at a wide range of 2θ angles to verify resolution and compute the instrumental contribution for structural adjustments. During the calcination/carbonation tests, XRD 5 min scans were continuously performed in a 20°-60° 2θ range with a step of 0.03° and 0.2 s step time. X-ray tube characteristics were 40 kV and 40 mA.

Topas 6 software from Bruker (Germany) was employed to fit the diffractograms recorded [44]. The relative content of the phases present in the sample (in wt%) was obtained by the Rietveld method [45,46] and their coherent crystal length (crystallite size) was determined using the Le Bail method [47,48]. For the refinements carried out by the Rietveld and Le Bail methods, the fundamental parameters method was applied with a detailed description of the diffractometer [44]. To achieve the best fit, zero error (2Θ) or sample displacement, as well as absorption and lattice parameters, were treated as adjustable parameters. Lorentz polarization geometric factors were used according to the configuration. Background adjustment was made by a fourth-order Chebyshev polynomial. The best and most correct combinations of Gaussian and Lorentzian functions were used for the calculation of the crystallite sizes. Robustness of the results derived and the possible discrepancy between observed values and expected was corroborated from several fitting indicators such as the goodness of fit (GOF) and residual factors (Rwp and RBragg) [46].

Samples morphology after the calcination/carbonation cycles was examined by means of scanning electron microscopy (SEM) micrographs using a FEI (USA) Teneo model equipment.

3. Results and discussion

Figure 3 shows a waterflow representation of the successive diffractograms recorded during the calcination/carbonation cycles carried out using limestone (Fig. 3a) and dolomite (Fig. 3b). Temperature in each cycle varies between 850 °C for carbonation (blue curves in Fig. 3) and 940 °C for calcination (red curves). The figures show the main Bragg peaks of the phases appearing in the cycles: calcite ($CaCO_3$: Rhombohedral, space group $R\bar{3}c$ (167)), lime (CaO: cubic, space group $Fm\bar{3}m$ (225)) and periclase (MgO: cubic, space group $Fm\bar{3}m$ (225)) in the case of dolomite also.

As reported in previous studies, dolomite decomposition under CO_2 is seen to occur through two steps at CO_2 partial pressures higher than 0.1 atm [27,49]. As temperature rises, the first decomposition step yields $CaCO_3$ and MgO. $CaCO_3$ decomposition into CaO and CO_2 occurs afterwards at a higher temperature depending on the CO_2 partial pressure:

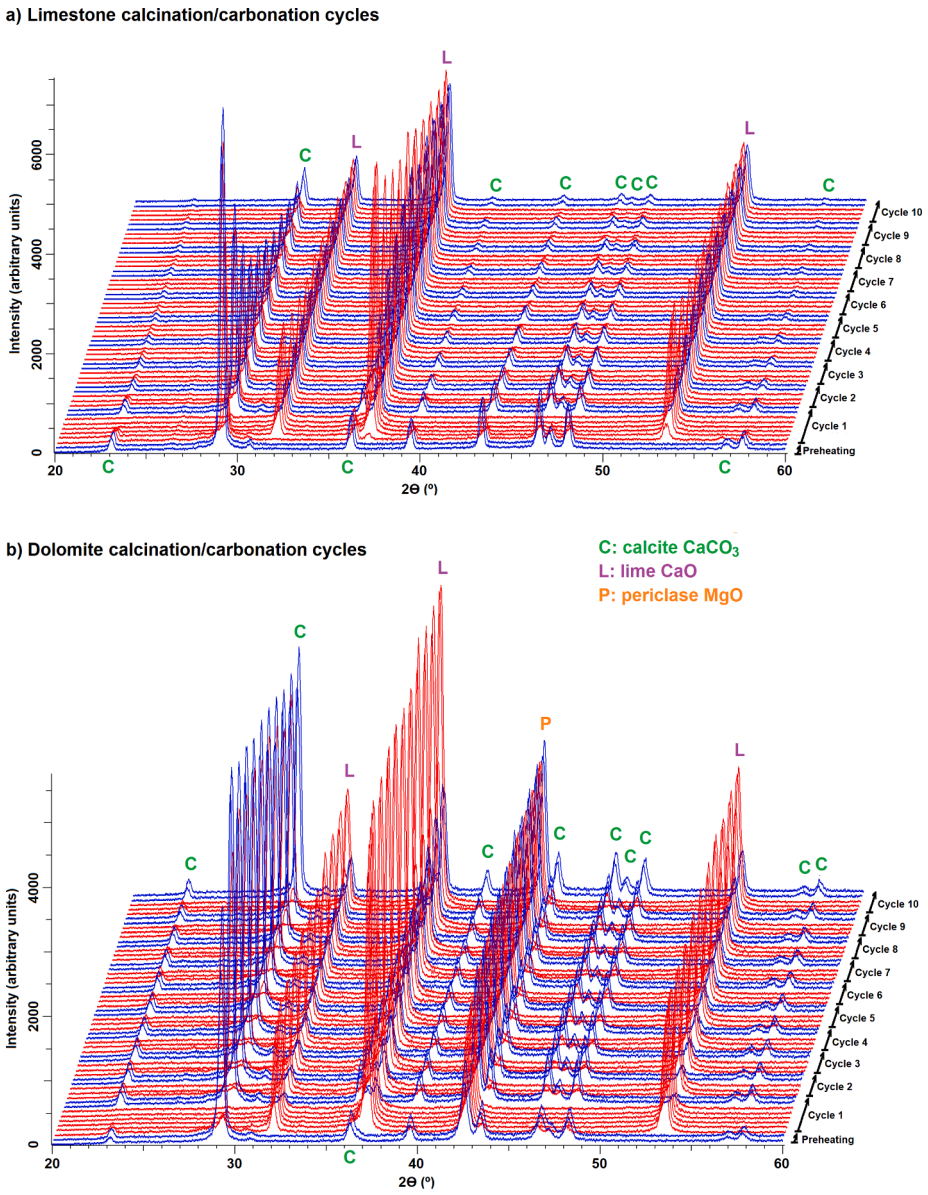

Fig. 3. Diffractograms recorded by *in situ* XRD analysis tests during calcination/carbonation cycles under CO_2 for limestone (a) and dolomite (b). Temperature is changed between 850 °C for carbonation (blue lines) and 940 °C for calcination (red lines). Main Bragg peaks of calcite C ($CaCO_3$: Rhombohedral, space group $R\bar{3}c$ (167)), periclase P (MgO: cubic, space group $Fm\bar{3}m$ (225)) and lime L (CaO: cubic, space group $Fm\bar{3}m$ (225)) are indicated.

$$CaMg(CO_3)_2 \rightarrow CaCO_3 + MgO + CO_2 \quad (2)$$

$$CaCO_3 \rightarrow CaO + CO_2 \quad (3)$$

TGA studies have shown that the intermediate decomposition of dolomite (Eq. (2)) is not significantly affected by the CO_2 partial pressure P whereas the decomposition of $CaCO_3$ (3) shifts to higher temperatures as the CO_2 partial pressure is increased [50,51] according to the thermodynamic equilibrium of the $CaCO_3$ calcination reversible reaction (4) [40,52]:

$$P(atm) \approx 4.083 \cdot 10^7 \cdot e^{\left(\frac{-20474}{Teq}\right)} \quad (4)$$

where Teq (in K) is the temperature for the calcination/carbonation reaction to be at thermodynamic equilibrium (3).

Dolomite decomposition under pure CO_2 at atmospheric pressure has been reported to start at around 700 °C [27,49,53]. Complete calcination through the second step (Eq. (3)) begins to occur above the equilibrium temperature for $CaCO_3$ decomposition under CO_2 at atmospheric pressure (Teq ~895 °C according to equation (4)) [27,49]. Experimental observations indicate that $CaCO_3$ decomposition in this second stage occurs at a significantly faster rate compared to $CaCO_3$ decomposition for limestone [49].

By increasing the temperature up to 850 °C under CO_2 in the preheating step of our experiments, dolomite is decomposed into MgO and $CaCO_3$. Interestingly, *in situ* XRD measurements reveal different behaviours regarding the volume of the unit cell of the $CaCO_3$ naturally present in limestone and the $CaCO_3$ formed during first step decomposition of dolomite (Eq. (2)). Fig. 4a shows the 2θ position of the $CaCO_3$ Bragg peaks registered at 850 °C in the preheating stage and the $CaCO_3$ formed after CaO carbonation in cycle 1. As can be seen, in the case of limestone the peaks appear exactly in the same 2θ position indicating that the cell structure volume remains constant. However, the Bragg peak of the $CaCO_3$ derived from dolomite first step decomposition (Fig. 4b) appears at a higher 2θ value compared with the Bragg peak of the $CaCO_3$ formed after carbonation in cycle 1. This indicates that the

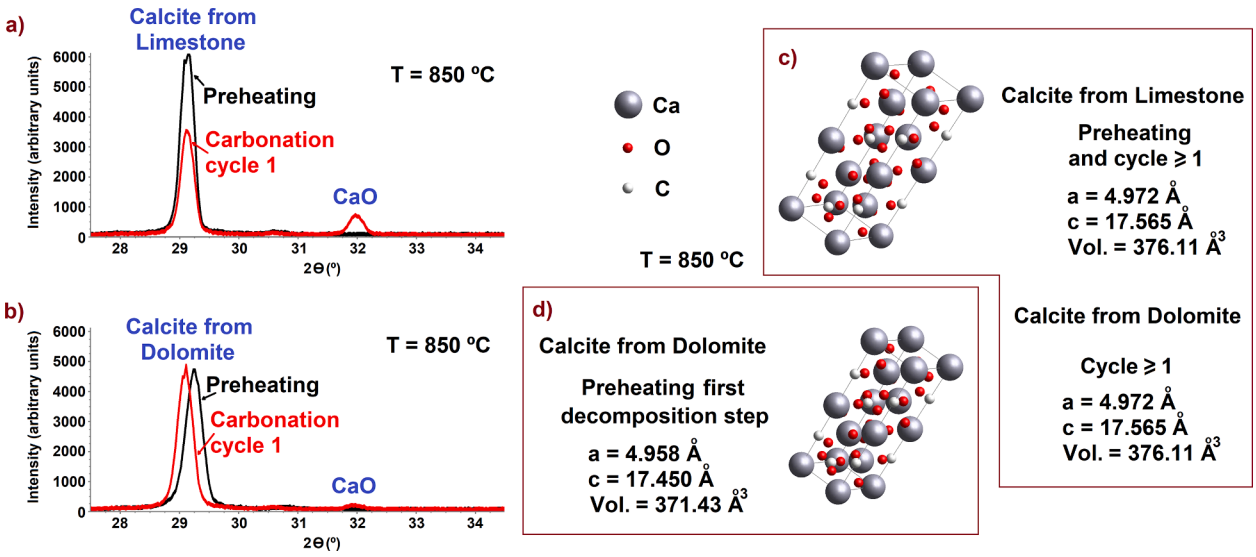

Fig. 4. Diffractograms obtained at 850 °C for $CaCO_3$ derived from limestone (a) and dolomite (b) in the preheating step at 850 °C and after carbonation in cycle 1. Lattice parameters, volume, and a representation of the unit cell at 850 °C obtained by Rietveld adjustments are indicated.

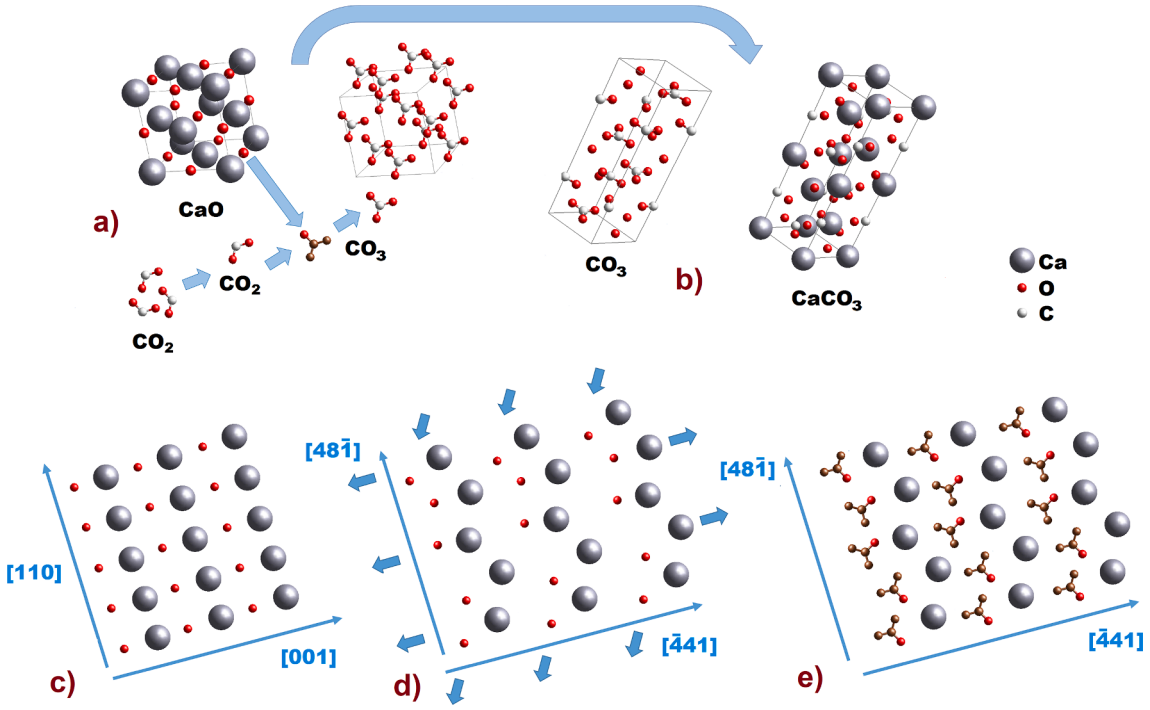

Fig. 5. Schematic representation of the crystallographic transformation of CaO to $CaCO_3$ during carbonation. (a) CaO structure (and same structure with hidden Ca atoms) indicating CO_2 adsorption process; (b) $CaCO_3$ structure with hidden Ca atoms and complete structure; (c) cubic structure of CaO in the $(1\bar{1}0)$ plane; (d) and (e) $(10\bar{1}4)$ calcite plane. In (d), the arrows mark the direction towards which Ca and O atoms move from the CaO structure. In (e), the CO_2 adsorbed molecule is colored.

$CaCO_3$ structure in the latter case is dilated and therefore the peaks move to lower 2θ values. Information on the lattice parameters obtained from Rietveld adjustments is detailed in Fig. 4. Arguably, this difference in $CaCO_3$ cell volume could play a role to lower the temperature at which full calcination is achieved for dolomite as compared to limestone as widely reported in the literature from TGA studies [4,54].

Figure 5 schematizes the evolution of the unit cell from CaO to $CaCO_3$ during carbonation under CO_2. In Fig. 5a, the unit cell of CaO is represented with all the atoms. The cell is depicted with only the C and O atoms after CO_3^{2-} ions placed in the same plane are formed. Ca atoms are not plotted for the sake of clarity to better illustrate the transformation. Fig. 5a also shows the CO_2 molecules before being adsorbed and the formation of CO_3^{2-} ions. The structure, once CO_2 is adsorbed, evolves towards the $CaCO_3$ structure shown in Fig. 5b. The unit cell of calcite ($CaCO_3$) is shown with only C and O atoms and with all the atoms. Fig. 5c shows the cubic structure of CaO in the $(1\bar{1}0)$ plane. $(10\bar{1}4)$ $CaCO_3$ plane is drawn in Fig. 5d and 5e. The arrows in Fig. 5d mark the direction towards which Ca and O atoms move from the CaO structure. CO_2 adsorbed molecules are coloured in Fig. 5e.

Figure 6 shows the multicycle evolution of the wt% (weight percentage) of the phases appearing along the calcination/carbonation cycles. Calculations are based on adjustments using the Rietveld

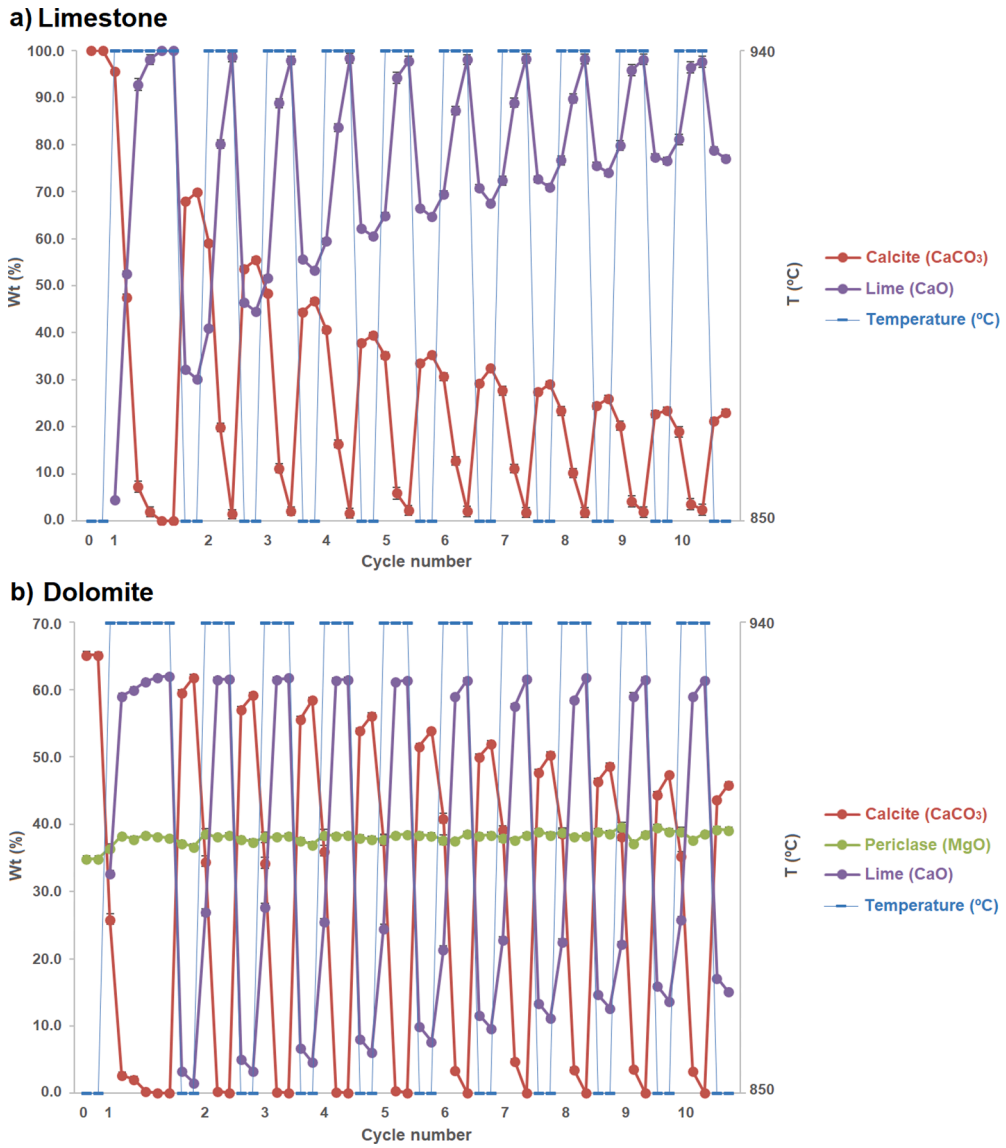

Fig. 6. Evolution with the cycle number of the wt% of phases present during the calcination/carbonation cycles for limestone (a) and dolomite (b).

method. In the case of limestone (Fig. 6a), during preheating to 850 °C there is only calcite ($CaCO_3$), which starts to decompose into lime (CaO) as the temperature is raised to the target calcination temperature (940 °C) taking about 20 min to decompose completely. Decomposition of the $CaCO_3$ naturally present in limestone is notably slower than decomposition of the $CaCO_3$ newly formed by CaO carbonation in subsequent cycles. From the second cycle, practically all the $CaCO_3$ is decomposed in about 15 min. When the temperature is decreased in the first cycle to 850 °C for carbonation, transformation of CaO into $CaCO_3$ is not fully achieved. Around 70 wt% of CaO is converted into $CaCO_3$ in this first cycle. In the following cycles, CaO conversion progressively decreases as can be seen in Fig. 6a. In cycle 10 approximately only 22 wt

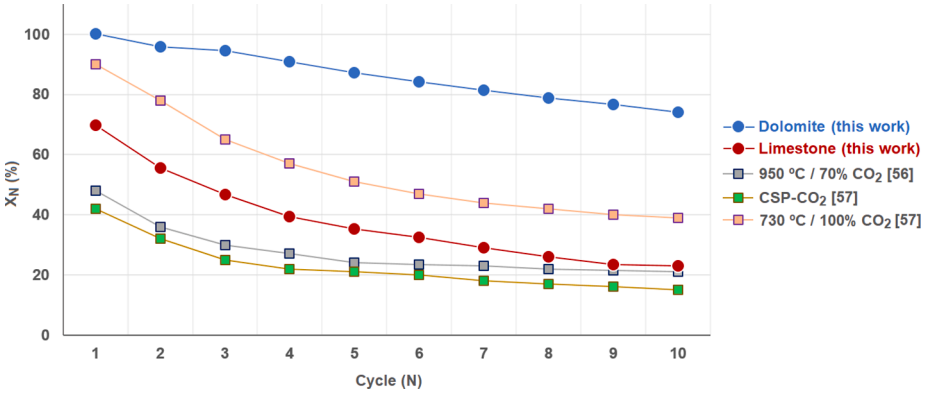

Fig. 7. Evolution with the cycle number of CaO conversion for dolomite and limestone. In this work X_N is obtained as $X_N = (CaCO_3\ wt\%)_N / (CaO\ wt\%)_N$ where CaO wt% and $(CaCO_3\ wt\%)_N$ are derived by Rietveld adjustment at the start and the end of the carbonation stage in cycle N. Data reported in the literature are plotted, derived from thermogravimetric measurements on limestone at diverse calcination/carbonation conditions. 950 °C / 70% CO_2 (calcination at 950 °C for 5 min, carbonation at 650 °C for 5 min) [56]; CSP-CO_2 (calcination at 750 °C for 5 min, carbonation at 850 °C for 5 min) [57]; 730 °C / 100% CO_2 (calcination at 730 °C for 10 min, carbonation at 850 °C for 5 min) [57].

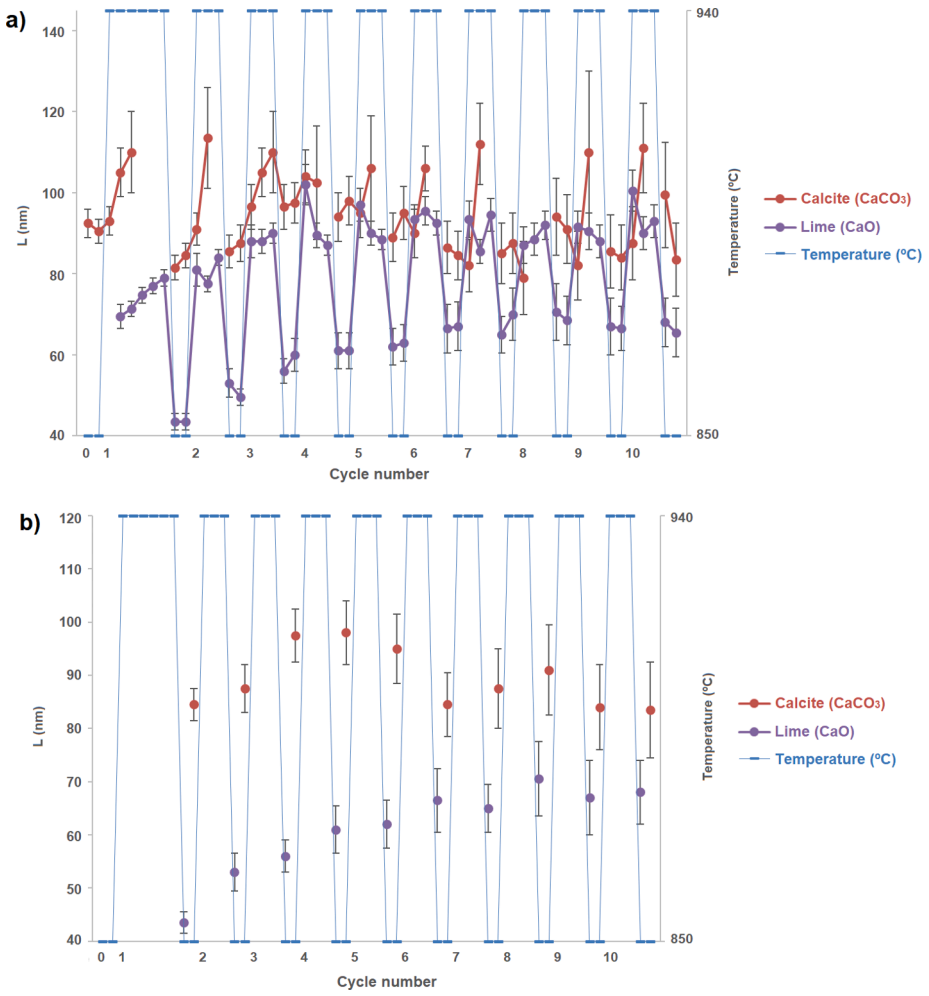

Fig. 8. (a) Evolution with the cycle number of the crystallite size calculated for calcite ($CaCO_3$) and lime (CaO) during calcination/carbonation cycles in the case of limestone. (b) shows only data for CaO at the beginning of carbonation and $CaCO_3$ at the end of carbonation for each cycle.

% of CaO is converted into $CaCO_3$. The progressive loss of CaO activity in the CaL process with the cycle number, as observed in our study, has been widely reported in the literature from TGA experiments [4,55].

As seen in Fig. 6b dolomite shows a well differentiated behaviour from limestone. Initially, during preheating from ambient to 850 °C, dolomite fully decomposes into $CaCO_3$ and periclase (MgO). The wt% of MgO remains constant in the rest of the cycles as would be expected since it is an inert compound at the conditions employed. During calcination in the first cycle at 940 °C full decomposition of $CaCO_3$ into CaO is achieved. In subsequent cycles, the $CaCO_3$ newly formed by CaO carbonation decomposes quickly into CaO. Remarkably, the degree of CaO conversion to $CaCO_3$ during the carbonation stage decreases much more slowly than in the case of limestone. Almost 100% CaO conversion is achieved in the first cycle. CaO conversion declines slowly reaching around 75% in cycle 10 as compared to only 22 wt% for limestone. Fig. 7 summarizes data extracted from Fig. 6 on the multicycle CaO conversion clearly showing the greater reactivity of dolomite derived CaO in comparison with CaO derived from limestone. This finding is consistent with the results reported in previous TGA studies [49]. Mitigation of the multicycle loss of CaO reactivity in the case of dolomite as compared to limestone has been related to the stabilizing role of inert MgO grains that would arguably minimize the aggregation and sintering of the nascent CaO grains in the calcination stage [4] albeit no quantitative data has been noninvasively measured to our knowledge on the multicycle evolution of CaO crystallite size. For comparison, and to show the consistency of our results with previously reported results, data reported in the literature [56,57] from thermogravimetric analysis are also plotted in Fig. 7. Note however that a direct quantitative comparison of the data is difficult since the results are highly sensitive to the conditions employed during the experiments as discussed in [56].

Figure 8 shows data for the crystallite size (L) calculated for $CaCO_3$ and CaO along the calcination/carbonation cycles in the case of limestone. Fig. 8a includes all the data, while in Fig. 8b the data corresponds to the crystallite size of CaO at the beginning of the carbonation stage and the crystallite size of $CaCO_3$ at the end of carbonation. The first value obtained for CaO would be the value just when reaching the temperature of 850 °C to start carbonation, while the second value for $CaCO_3$ would be the value obtained once crystal growth has stabilized at 850 °C at the end of carbonation. As can be seen in Fig. 8b, the CaO crystallite size in the beginning of carbonation increases from a value of 43 nm in cycle 1 to stabilize from the 7th cycle around 68 nm. On the other hand, $CaCO_3$ crystallite size at the end of carbonation generally remain stable around 85–95 nm.

Data on the crystallite size obtained for $CaCO_3$ and CaO (Fig. 8a) are separately shown in Fig. 9a and 9b, respectively for the sake of clarity. The $CaCO_3$ that starts to form at the beginning of carbonation has a crystallite size ranging between approximately 80 and 95 nm, which remains roughly constant during carbonation. In the calcination stage the $CaCO_3$ crystallite size generally increases from around 80–95 nm at the beginning of the calcination to about 105–115 nm at the end of the calcination stage. This same trend is observed in all the cycles. Thus, $CaCO_3$ sintering occurs mostly in the calcination stage albeit $CaCO_3$

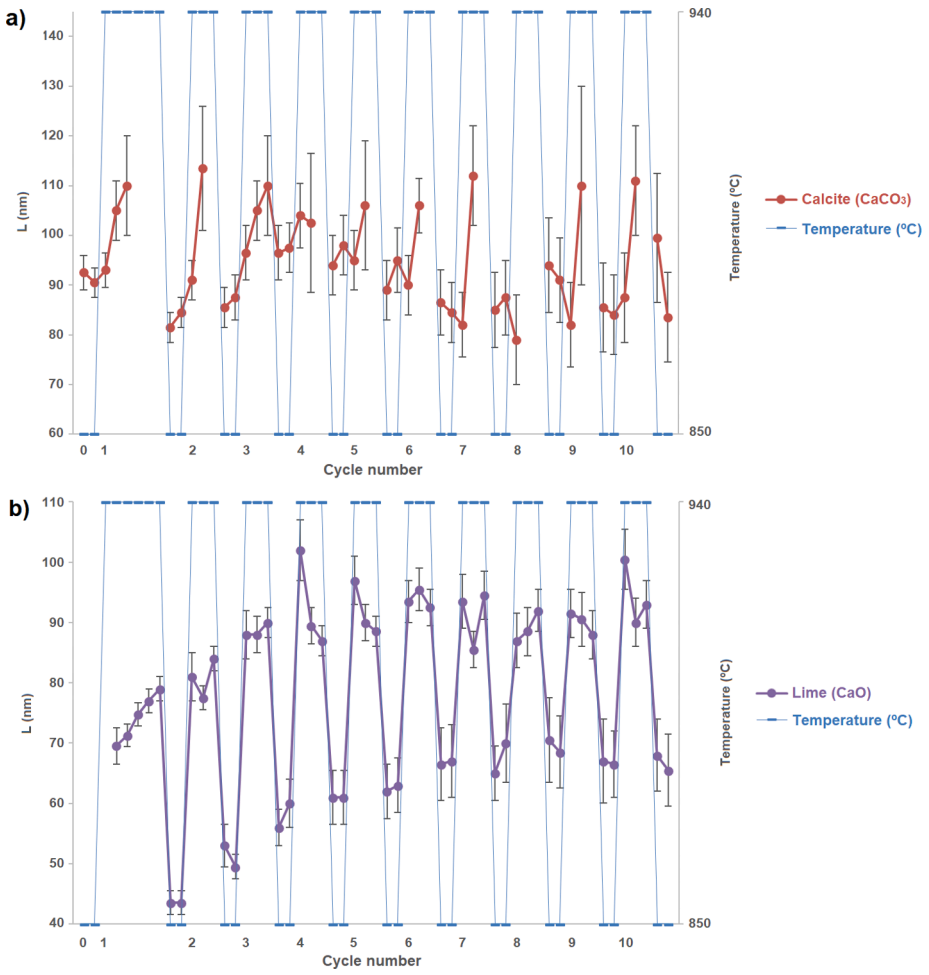

Fig. 9. Multicycle evolution of crystallite size calculated for calcite ($CaCO_3$) (a) and lime (CaO) (b) during calcination/carbonation tests in the case of limestone.

decomposition is fully achieved at the end of calcination. Fig. 9b shows the multicycle evolution of the CaO crystallite size. Since carbonation is incomplete, a fraction of unreacted CaO remains after carbonation in the calcination stage where it suffers a severe sintering. As may be seen in Fig. 9b, CaO crystallite size at the beginning of calcination in cycle 1 has a size of about 70 nm and grows up to ~80 nm. Once calcination is finished, CaO crystallite size decreases to around 44 nm. This size is an average of the crystallite sizes of the sintered CaO in the previous calcination stage and the newly formed CaO by $CaCO_3$ decomposition. From cycle 2 to cycle 6, a similar behaviour is observed with a clear-cut drop from the end of the calcination stage to the beginning of carbonation. Thus, the data indicates that CaO sintering is mostly experienced by the fraction of unreacted CaO that remains in the calcination stage. This fraction increases progressively with the number of cycles and as a

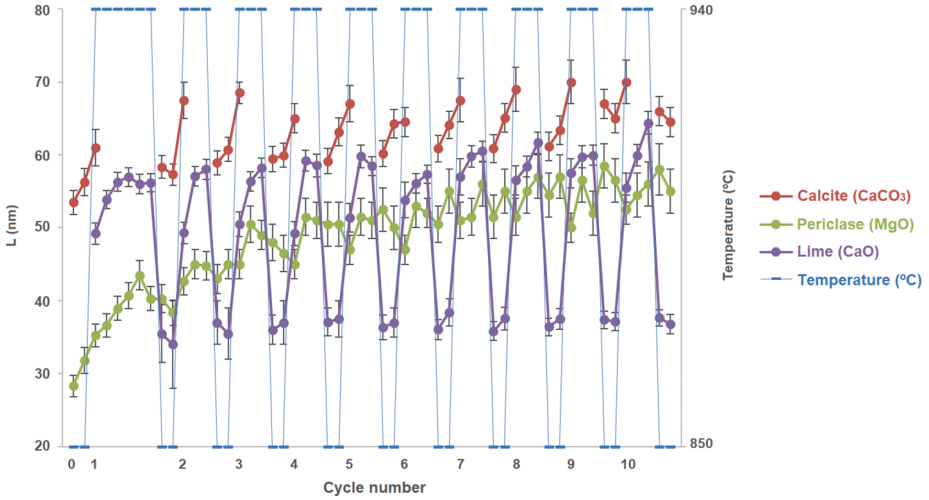

Fig. 10. Evolution with the cycles of the crystallite size obtained for calcite ($CaCO_3$), periclase (MgO) and lime (CaO) during calcination/carbonation tests under CO_2 performed on dolomite.

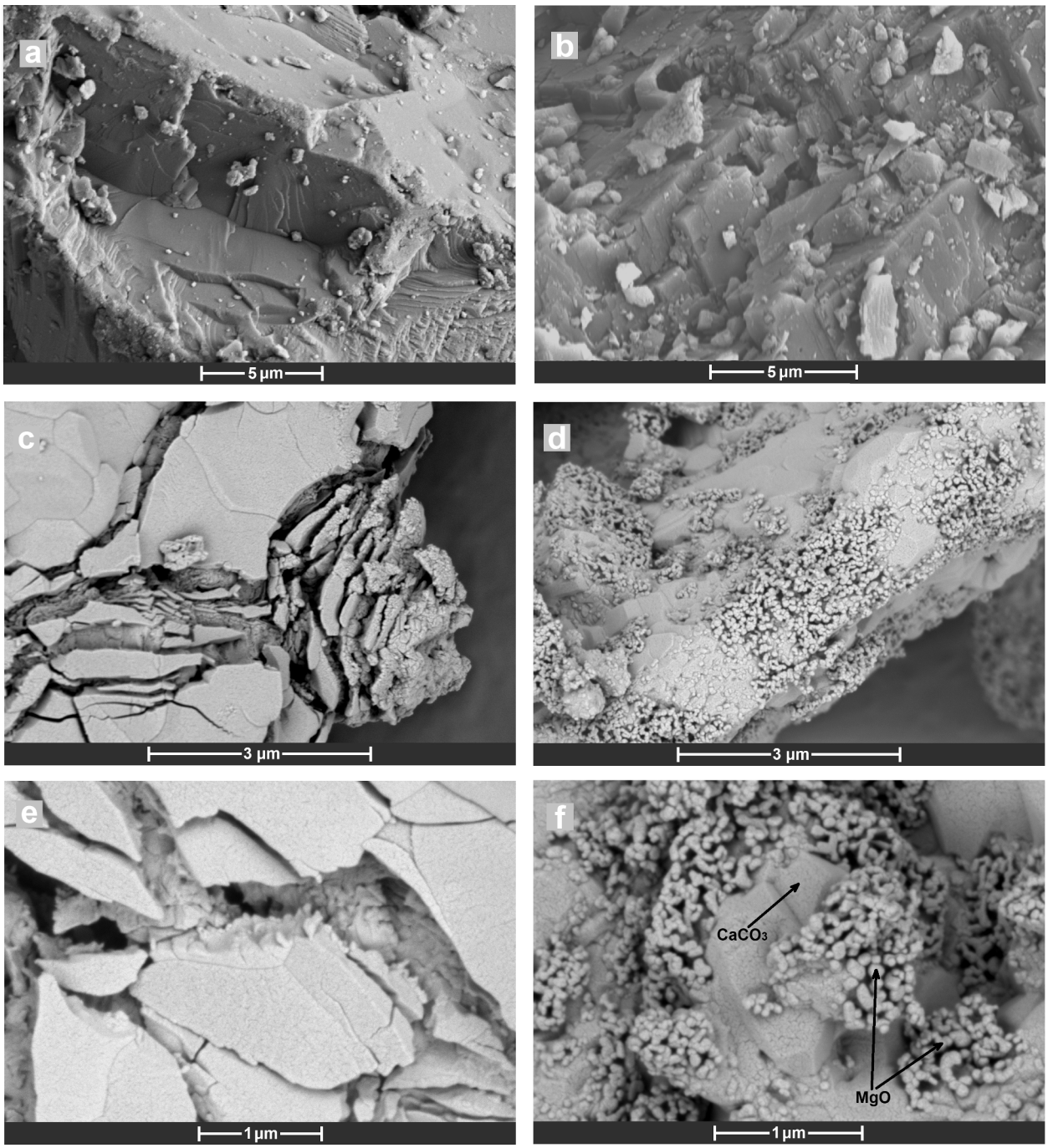

Fig. 11. SEM micrographs of limestone (c, e) and dolomite (d, f) after the calcination/carbonation cycles. Fresh limestone (a) and dolomite (b) images are also shown for comparison.

consequence CaO reactivity is further hindered. On the other hand, the CaO formed by $CaCO_3$ calcination has a small crystal size. As CaO conversion is decreased, the fraction of this newly formed CaO also decreases progressively with the number of cycles. CaO sintering is thus mainly caused by incomplete conversion from the first cycle, which leaves a fraction of poorly reactive CaO for carbonation in the following cycle. This effect is progressively enhanced in subsequent cycles leading to a marked decline of CaO conversion. It is worth to remark also that $CaCO_3$ suffers severe sintering before decarbonation since the carbonation temperature is well above the $CaCO_3$ Tamman temperature (around 550 °C) [58]. However, the carbonation reactivity of CaO is directly correlated to the area of CaO available for carbonation [52], and it is not expected that a high level of sintering of $CaCO_3$ will lead to a low surface area of the CaO formed during calcination. Thermogravimetric analysis reported in the literature carried out at conditions for CO_2 capture where carbonation was performed at a relatively lower temperature (around 650 °C) [59,60] suggest that $CaCO_3$ sintering is not the major contributor to a decline of the CaO surface area available for carbonation in the next cycle. In these works, a recarbonation stage was introduced just after carbonation and before the calcination stage. The recarbonation stage was carried out at high CO_2 concentration and high temperature (800 °C). The goal of introducing this recarbonation stage was to achieve near full carbonation of the CaO that remained unreacted at the end of the short carbonation stage at 650 °C. Despite that the conditions in this recarbonation stage were indeed prone to severe $CaCO_3$ sintering the results showed a mitigation of the loss of CaO

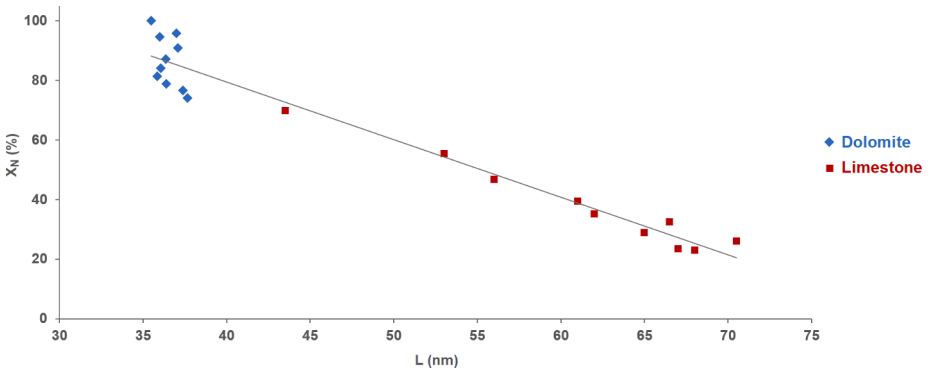

Fig. 12. CaO crystallite size (nm) versus CaO conversion (%) measured in our study for dolomite and limestone.

activity in the next cycle. These studies uphold our argument that the decline of CaO carbonation activity with the number of cycles is arguably attributable to the progressive sintering during the calcination stage of the CaO that remained unreacted during carbonation.

Figure 10 shows calculated data for the crystallite size of $CaCO_3$, MgO and CaO derived from the diffractograms recorded during the calcination/carbonation cycles for dolomite. Generally, the size of the crystallites is around 30 nm smaller for both $CaCO_3$ and CaO in comparison with limestone. As may be seen in Fig. 10 the crystallite size of the inert MgO grains formed during the initial dolomite decomposition increases monotonically, which is consistent with SEM observations showing a progressive aggregation and growth of the MgO grains [61]. The growth of MgO grain size and its segregation from CaO as the cause of the loss of CaO activity with the number of cycles has been already discussed in previous thermogravimetric studies [4,16,28]. Fig. 11 shows micrographs of limestone and dolomite samples after the cycles. In the case of limestone (Fig. 11c and Fig. 11e), the particles appear fractured arguably due to heat stresses. Particle fracturing or attrition can be a serious issue in the practical application since fine powders can be easily elutriated by the gas flow [62]. Fig. 11a shows also a SEM image of fresh limestone, where these fractures are not visible. In the case of dolomite (Fig. 11d and Fig. 11f) $CaCO_3$ and MgO grains can be clearly distinguishable. Moreover, it may be seen that MgO grains are aggregated after the cycles and segregated from the carbonate substrate. The growth and aggregation of MgO grains would lead to a loss of their hindrance effect on the growth of CaO crystallite size by sintering as argued in previous studies [49]. In contrast with limestone, particle fracturing is not observed in the SEM pictures of dolomite after the cycles. Thus, the presence of MgO grains confers the structure with both thermal and mechanical resistance which would lead to a superior performance in the CaL process. Regarding CaO crystallite size in the carbonation stage it remains roughly constant with the cycles around 37 nm (Fig. 10) in contrast with the growth observed for the crystallite size of limestone derived CaO (Fig. 9). Since CaO crystallite size can be directly related to its reactivity [4,49]. This observation would explain the higher and more stable CaO conversion measured for dolomite derived CaO as compared to CaO derived from limestone. During the calcination stage the crystallite size of the $CaCO_3$ (previously formed by CaO carbonation) and of the remaining unreacted CaO grow as seen in Fig. 10. However, CaO reactivity is not significantly hindered as seen for limestone since the fraction of unreacted CaO is small and grows slowly with the cycle number. Fig. 12 shows that, as hypothesized in previous works, there is an inverse correlation between CaO conversion and the evolution of the CaO crystallite size. Interestingly, this trend is roughly the same trend for both materials. Our study demonstrates quantitatively, for the first time to our knowledge, this arguably universal relationship. Additional studies on other Ca-based materials would be needed though to confirm it.

Computational ab initio simulations have suggested that the nucleation of $CaCO_3$ on the CaO surface as initial step for carbonation is more favorable on the CaO (1 1 1) crystal planes, with CO_3^{2-} groups spreading laterally layer-by-layer in preference to nucleation on the (1 0 0) CaO planes [37]. In a previous work by the same authors on the nucleation mechanisms of $CaCO_3$ on CaO using energy criteria (instead of a steric insight), the (1 0 0) CaO planes were however identified as more energetically favourable for the nucleation of $CaCO_3$ on the CaO surface in

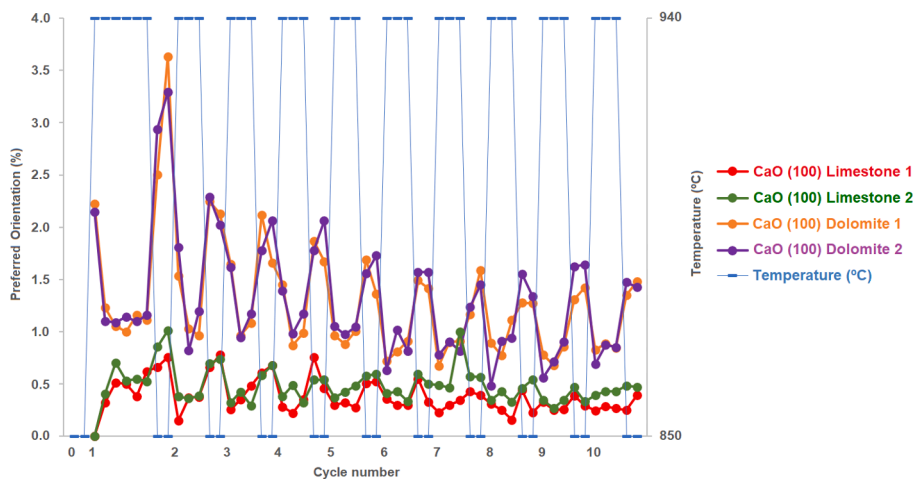

Fig. 13. Evolution with the cycles of the preferred orientation percentage in the CaO (1 0 0) plane along the calcination/carbonation cycles for limestone (a) and dolomite (b). Results for two independent tests on each sample are plotted to demonstrate data reproducibility.

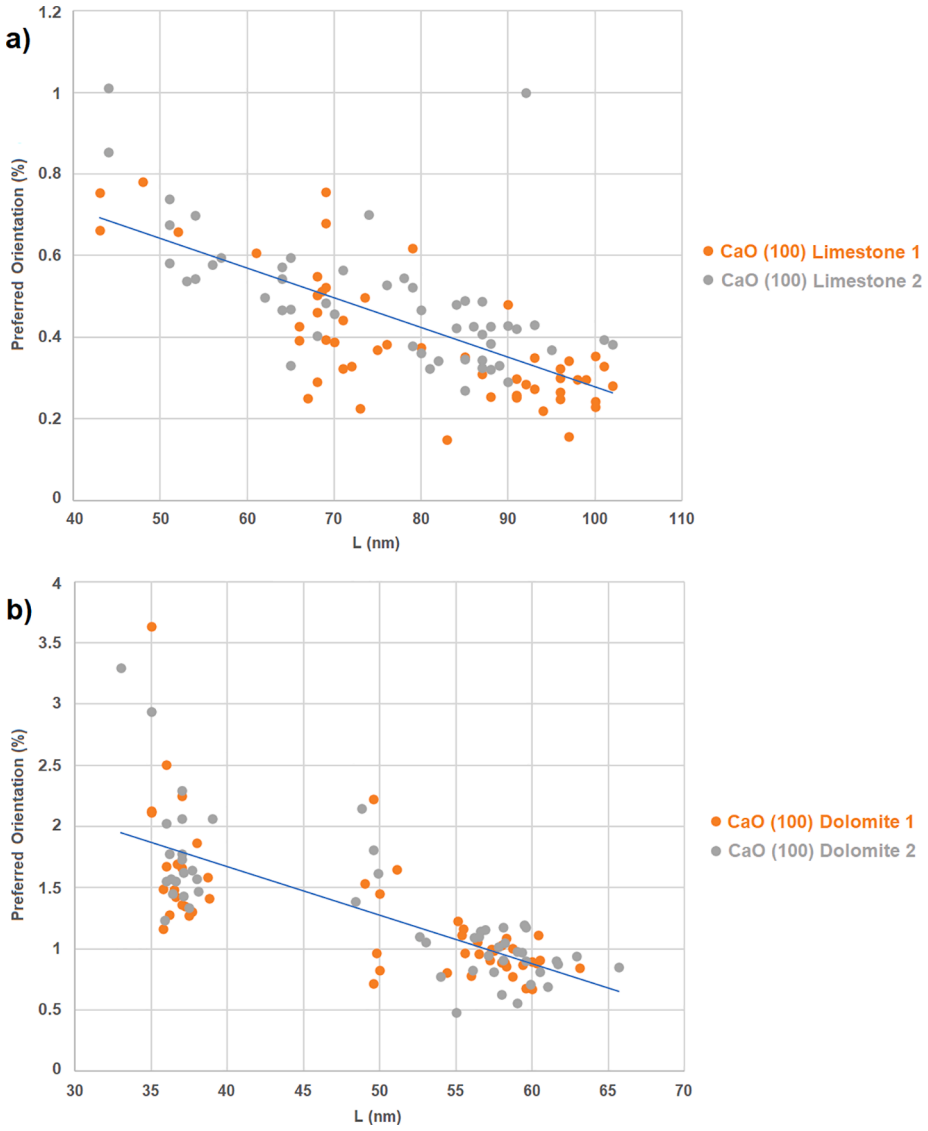

Fig. 14. Preferred orientation (%) in the CaO (1 0 0) plane as a function of CaO crystallite size for the multicycle tests carried out using limestone (a) and dolomite (b). Results from two independent tests on each sample are plotted to demonstrate data reproducibility.

comparison with the (1 1 1) and (1 1 0) CaO planes [38]. Accordingly, the preferential growth of the nascent CaO crystals during calcination in determined planes could be a mechanism contributing to the multicyclic loss of CaO reactivity although experimental evidences on this argument are still lacking. Thus, the study of $CaCO_3$ nucleation is of vital importance to understand the evolution of the multicycle CaO activity. Likewise, it is equally relevant to get a grip on the process of decomposition of $CaCO_3$ to form CaO to further understand the multicycle evolution of CaO reactivity.

The present in-situ XRD analysis allows studying the crystallographic preferred orientations of CaO as the number of cycles progresses for the CaO (1 0 0), (1 1 0) and (1 1 1) planes. Crystallographic preferred orientations were calculated for the CaO planes (1 0 0) and (1 1 0) from their homologues (2 0 0) and (2 2 0), respectively. Additionally, the evolution with the cycles of the preferred orientations of the $CaCO_3$ (1 0 4) plane was also analysed. To this end, the March-Dollase approximation has been used [63,64]. The percentage of preferred orientation was calculated using equation (5) from the March parameter and Rietveld adjustments [44,65]:

$$PO(\%) = 100\% \left[\frac{(1-r)^3}{1-r^3} \right]^{\frac{1}{2}} \quad (5)$$

Where *PO(%)* represents the percentage of preferred orientation and *r* is the March parameter [65]. The results show that practically only the CaO (1 0 0) plane has preferred orientations of significant values. Fig. 13 shows the results obtained on the percentage of preferred orientation in the CaO (1 0 0) plane during the multicycle tests for both limestone and dolomite (Fig. 13). In general, a higher orientation is observed at 850 °C in the carbonation stage and a lower orientation at 940 °C during calcination. Nonetheless, the orientation is not significant albeit it is slightly higher for dolomite compared to limestone, with a tendency to decrease with the number of cycles. Interestingly, the CaO (1 0 0) plane preferred orientation oscillates along the cycles. It increases in the carbonation stage and decreases during calcination. This result would suggest that the nascent CaO grows during calcination preferentially in the (1 0 0) planes. On the other hand, nucleation of $CaCO_3$ during carbonation would take place preferentially on the (1 1 1) planes thus reducing the (1 0 0) preferred orientation. This mechanism would be more apparent in the case of dolomite where CaO conversion is higher,

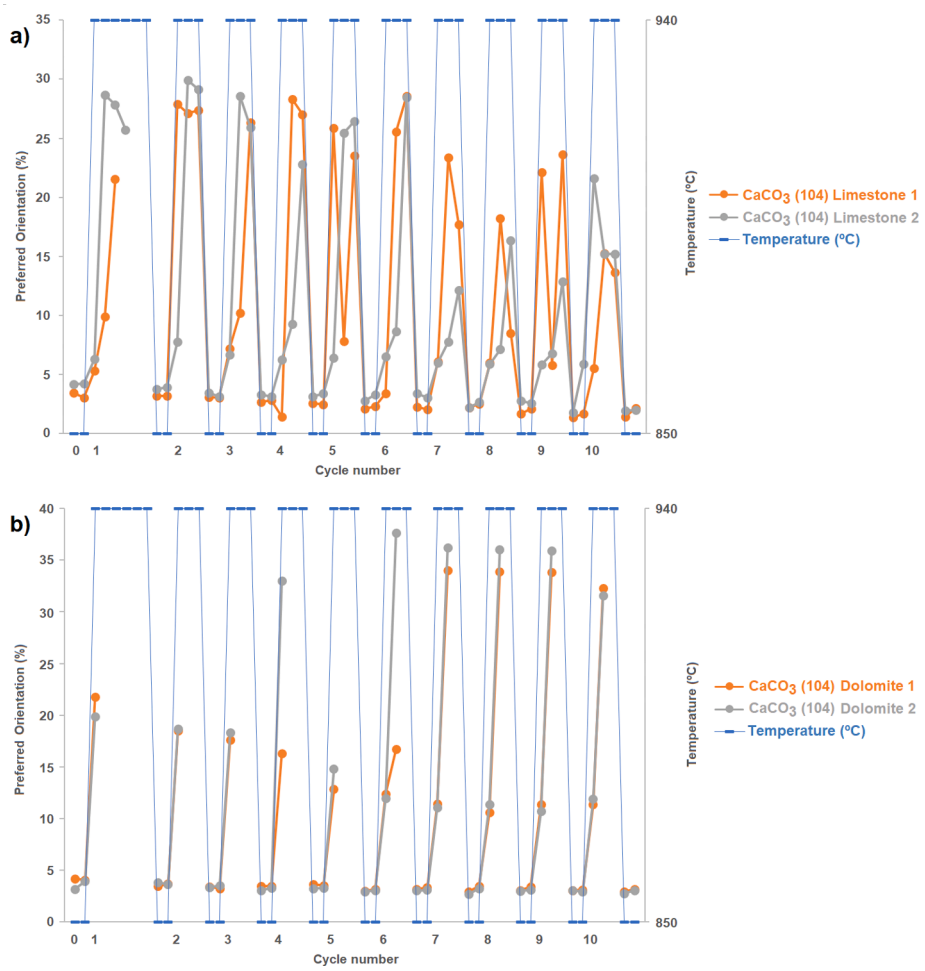

Fig. 15. Evolution with the cycles of preferred orientation percentage in the $CaCO_3$ (1 0 4) plane calculated for limestone (a) and dolomite (b). Results from two independent tests are plotted to demonstrate data reproducibility.

which would explain the higher values of preferred orientation seen in Fig. 13 for dolomite.

Figure 14 shows the preferred orientation in the CaO (1 0 0) plane as a function of the CaO crystallite size calculated along the multicycle calcination/carbonation tests for limestone (Fig. 14a) and for dolomite (Fig. 14b). As may be observed there is a decreasing trend of the CaO (1 0 0) preferred orientation as the crystallite size increases. This may indicate that although the newly formed CaO by $CaCO_3$ decarbonation in the calcination stage of each cycle has a preferred orientation in the (1 0 0) plane, the CaO that remains unreacted after carbonation and sinters in the following calcination stage loses the preferred orientation as the crystal size is increased. In this way the overall CaO (1 0 0) preferred orientation declines with the number of cycles. The progressive loss of CaO reactivity towards carbonation could be thus related to the decrease of CaO preferred orientation in the (1 0 0) plane associated to the enlargement of crystallite size during calcination of the unreacted CaO.

Figure 15 shows the results obtained for the preferred orientation of the $CaCO_3$ (1 0 4) plane. As can be seen, a noticeable preferred orientation of this plane is obtained. In general, for both limestone and dolomite, a higher orientation occurs in the calcination stage as compared to carbonation. As seen for the CaO (1 0 0) plane, the preferred orientation of the $CaCO_3$ (1 0 4) plane oscillates along the cycles. It clearly increases in the calcination stage where $CaCO_3$ decomposition occurs and is decreased during carbonation when $CaCO_3$ is formed indicating that the (1 0 4) orientation is not privileged in the $CaCO_3$ layer that forms on the surface of the CaO grains. Fig. 16 shows data on the $CaCO_3$ crystallite size as a function of the preferred orientation in the (1 0 4) plane for limestone (Fig. 16a) and dolomite (Fig. 16b). For this plane, a trend is not as evident as in the case of the CaO (1 0 0) plane (Fig. 14) and there is generally a greater data dispersion for both the limestone and dolomite samples. For the carbonation stage, as in the case of the CaO (1 0 0) plane there is a slightly decreasing trend of the $CaCO_3$ (1 0 4) plane preferred orientation as the crystallite size increases, which is more apparent for dolomite than for limestone.

As reported in previous studies, the $CaCO_3$ layer that forms on CaO during carbonation would be in the range of 20 to 90 nm [35,66–68]. In our work, the penetration of the X-rays in the sample has been estimated using the AbsorbDX software from Bruker to assess if the present or nascent phases are being evaluated only on their surface or if the external layers are being penetrated. The penetration for limestone would be of the order of 186 nm for pure calcite at 850 °C and 131 nm at 940 °C for pure CaO. The penetration for dolomite would be 212 nm at 850 °C with calcite and MgO, with an estimated value of 186 nm when there is only MgO and CaO at 940 °C. Thus, the preferred orientations analysed above provide information on both CaO and $CaCO_3$ phases at the same time beyond the thickness of the $CaCO_3$ layer formed in the carbonation process.

4. Conclusions

The Calcium Looping process has been analysed in the present work for the first time to our knowledge by means of *In-situ* X-ray diffraction analysis. Natural limestone and dolomite samples have been subjected

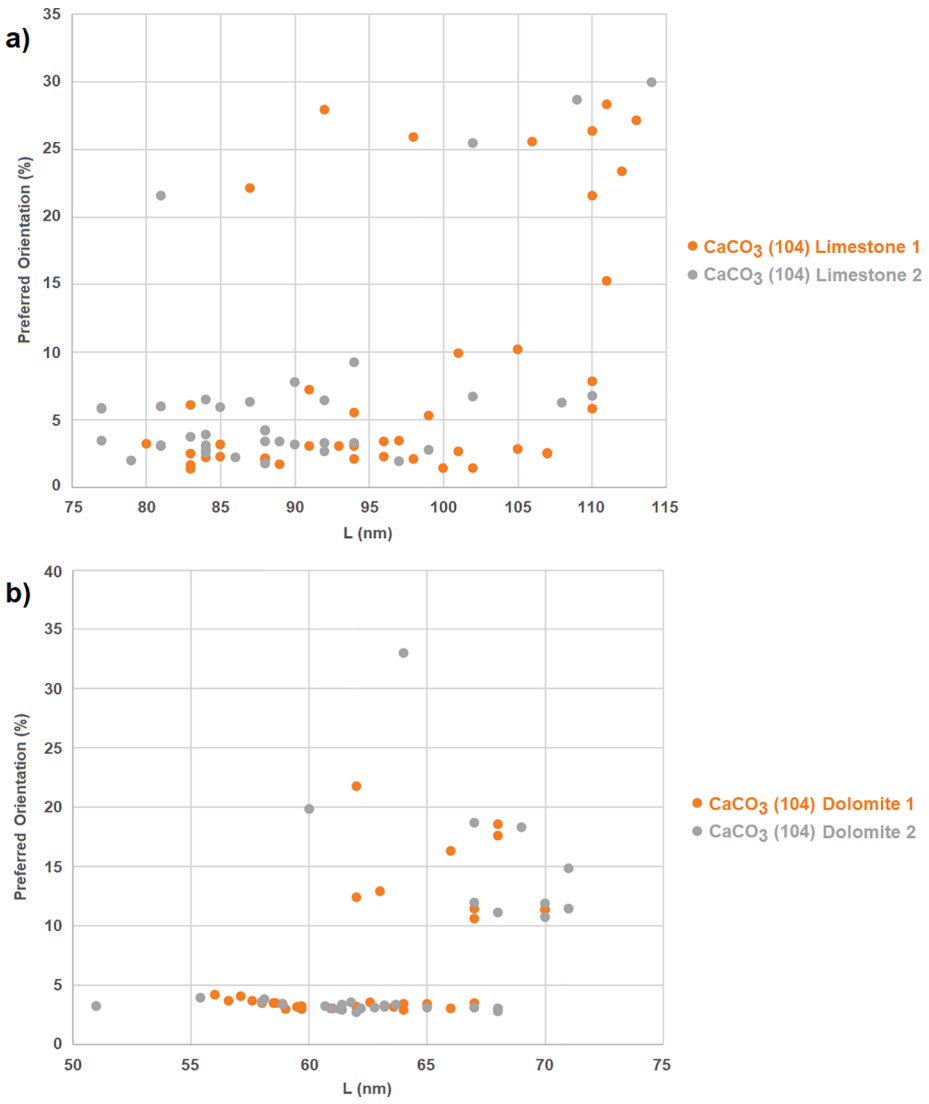

Fig. 16. Preferred orientation (%) in the $CaCO_3$ (1 0 4) plane as a function of $CaCO_3$ crystallite size along the multicycle tests for limestone (a) and dolomite (b). Results from two independent tests are plotted to demonstrate data reproducibility.

to calcination/carbonation cycles at optimum conditions for thermochemical energy storage..

CaO derived from dolomite decomposition shows a significantly greater multicycle reactivity compared to limestone derived CaO. After 10 cycles, dolomite still has a high reactivity. The *in-situ* XRD analysis presented in this manuscript has revealed some key features to further understand this behaviour.

The multicycle evolution of CaO and $CaCO_3$ crystallite sizes for dolomite is diverse from limestone, with a size of the crystallites smaller for dolomite. In the case of $CaCO_3$, both in limestone and dolomite, the crystallites have a smaller size at the beginning of CaO carbonation when $CaCO_3$ starts to be formed growing up as the carbonation stage progresses. CaO carbonation is not fully achieved in the short residence times employed as needed for practical applications. Consequently, part of the CaO remains unreacted in the calcination stage. The crystallite size of this unreacted CaO increases notably during calcination, which leads to a loss of its reactivity towards carbonation in the following carbonation stage. As the number of cycles is increased the fraction of unreacted CaO with enlarged crystal size and poor reactivity is increased over the CaO nascent from $CaCO_3$ decomposition during calcination. This leads to a progressive decline of the overall CaO multicycle activity. The presence of inert MgO grains in the case of dolomite formed during its initial decomposition mitigates the aggregation and sintering of CaO crystals. Thus, CaO conversion is almost fully achieved in the first cycles, which leads to a slower decline of the CaO multicycle activity. As the number of cycles is increased the crystal size of MgO increases monotonically and MgO grains segregate from the carbonate substrate therefore losing their hindrance effect to limit CaO crystal aggregation and growth.

Crystallographic preferred orientations have been analysed in our work for CaO in the planes (1 0 0), (1 1 0) and (1 1 1) and for $CaCO_3$ in the plane (1 0 4). Significant preferential orientation values have been obtained for the CaO (1 0 0) plane and for the $CaCO_3$ (1 0 4) plane during the calcination/carbonation cycles on both limestone and dolomite. The CaO (1 0 0) plane shows a higher orientation in the carbonation stage and it decreases in the calcination stage. An inverse correlation has been observed between the growth of the CaO crystallite size with the number of cycles and the CaO (1 0 0) plane preferred orientation.

Declaration of Competing Interest

The authors declare that they have no known competing financial interests or personal relationships that could have appeared to influence the work reported in this paper.

Acknowledgements

This work was supported by Spanish Government Agency Ministerio de Economía y Competitividad (contract No. CTQ2017-83602-C2-2-R, FEDER funds) and Junta de Andalucía-Consejería de Economía y Conocimiento (I + D + i FEDER Andalucía 2014-2020, contract no. US-1262507). We gratefully acknowledge the X-ray service of the Innovation, Technology and Research Center of the University of Seville (CITIUS).

References

[1] P. Pardo, A. Deydier, Z. Anxionnaz-Minvielle, S. Rougé, M. Cabassud, P. Cognet, A review on high temperature thermochemical heat energy storage, Renew. Sustain. Energy Rev. 32 (2014) 591–610, https://doi.org/10.1016/j.rser.2013.12.014.

[2] T.X. Li, S. Wu, T. Yan, J.X. Xu, R.Z. Wang, A novel solid-gas thermochemical multilevel sorption thermal battery for cascaded solar thermal energy storage, Appl. Energy 161 (2016) 1–10, https://doi.org/10.1016/j.apenergy.2015.09.084.

[3] H.L. Zhang, J. Baeyens, J. Degrève, G. Cacères, Concentrated solar power plants: review and design methodology, Renew. Sustain. Energy Rev. 22 (2013) 466–481, https://doi.org/10.1016/j.rser.2013.01.032.

[4] J.M. Valverde, P.E. Sanchez-Jimenez, L.A. Perez-Maqueda, Ca-looping for postcombustion CO_2 capture: a comparative analysis on the performances of dolomite and limestone, Appl. Energy 138 (2015) 202–215, https://doi.org/10.1016/j.apenergy.2014.10.087.

[5] R. Chacartegui, A. Alovisio, C. Ortiz, J.M. Valverde, V. Verda, J.A. Becerra, Thermochemical energy storage of concentrated solar power by integration of the calcium looping process and a CO_2 power cycle, Appl. Energy 173 (2016) 589–605, https://doi.org/10.1016/j.apenergy.2016.04.053.

[6] E.A. Mikhailova, C.J. Post, M.A. Schlautman, G.R. Groshans, M.P. Cope, L. Zhang, A systems-based approach to ecosystem services valuation of various atmospheric calcium deposition flows, Resources 8 (2019) 1–14, https://doi.org/10.3390/resources8020066.

[7] M.C. Romano, I. Martínez, R. Murillo, B. Arstad, R. Blom, D.C. Ozcan, H. Ahn, S. Brandani, Process simulation of Ca-looping processes: review and guidelines, Energy Procedia 37 (2013) 142–150, https://doi.org/10.1016/j.egypro.2013.05.095.

[8] S.E.B. Edwards, V. Materić, Calcium looping in solar power generation plants, Sol. Energy 86 (9) (2012) 2494–2503, https://doi.org/10.1016/j.solener.2012.05.019.

[9] K.G. Sakellariou, G. Karagiannakis, Y.A. Criado, A.G. Konstandopoulos, Calcium oxide based materials for thermochemical heat storage in concentrated solar power plants, Sol. Energy 122 (2015) 215–230, https://doi.org/10.1016/j.solener.2015.08.011.

[10] G.R. Groshans, E.A. Mikhailova, C.J. Post, M.A. Schlautman, M.P. Cope, L. Zhang, Ecosystem services assessment and valuation of atmospheric magnesium deposition, Geoscience 9 (2019) 1–13, https://doi.org/10.3390/geosciences9080331.

[11] K.E. N'Tsoukpoe, H. Liu, N. Le Pierrès, L. Luo, A review on long-term sorption solar energy storage, Renew. Sustain. Energy Rev. 13 (9) (2009) 2385–2396, https://doi.org/10.1016/j.rser.2009.05.008.

[12] T.M.I. Mahlia, T.J. Saktisahdan, A. Jannifar, M.H. Hasan, H.S.C. Matseelar, A review of available methods and development on energy storage; technology update, Renew. Sustain. Energy Rev. 33 (2014) 532–545, https://doi.org/10.1016/j.rser.2014.01.068.

[13] J.M. Valverde, J. Miranda-Pizarro, A. Perejón, P.E. Sánchez-Jiménez, L.A. Pérez-Maqueda, Calcium-Looping performance of steel and blast furnace slags for thermochemical energy storage in concentrated solar power plants, J. CO2 Util. 22 (2017) 143–154, https://doi.org/10.1016/j.jcou.2017.09.021.

[14] M. Benitez-Guerrero, J.M. Valverde, A. Perejon, P.E. Sanchez-Jimenez, L.A. Perez-Maqueda, Low-cost Ca-based composites synthesized by biotemplate method for thermochemical energy storage of concentrated solar power, Appl. Energy 210 (2018) 108–116, https://doi.org/10.1016/j.apenergy.2017.10.109.

[15] C. Ortiz, J.M. Valverde, R. Chacartegui, L.A. Perez-Maqueda, Carbonation of Limestone derived CaO for thermochemical energy storage: from kinetics to process integration in concentrating solar plants, ACS Sustain. Chem. Eng. 6 (5) (2018) 6404–6417, https://doi.org/10.1021/acssuschemeng.8b00199.

[16] B. Sarrión, A. Perejón, P.E. Sánchez-Jiménez, L.A. Pérez-Maqueda, J.M. Valverde, Role of calcium looping conditions on the performance of natural and synthetic Ca-based materials for energy storage, J. CO2 Util. 28 (2018) 374–384, https://doi.org/10.1016/j.jcou.2018.10.018.

[17] Y. Da, Y. Xuan, L. Teng, K. Zhang, X. Liu, Y. Ding, Calcium-based composites for direct solar-thermal conversion and thermochemical energy storage, Chem. Eng. J. 382 (2020) 122815, https://doi.org/10.1016/j.cej.2019.122815.

[18] S. Yasipourtehrani, S. Tian, V. Strezov, T. Kan, T. Evans, Development of robust CaO-based sorbents from blast furnace slag for calcium looping CO_2 capture, Chem. Eng. J. 387 (2020) 124140, https://doi.org/10.1016/j.cej.2020.124140.

[19] A. Alovisio, R. Chacartegui, C. Ortiz, J.M. Valverde, V. Verda, Optimizing the CSP-calcium looping integration for thermochemical energy storage, Energy Convers. Manag. 136 (2017) 85–98, https://doi.org/10.1016/j.enconman.2016.12.093.

[20] C. Ortiz, R. Chacartegui, J.M. Valverde, A. Alovisio, J.A. Becerra, Power cycles integration in concentrated solar power plants with energy storage based on calcium looping, Energy Convers. Manag. 149 (2017) 815–829, https://doi.org/10.1016/j.enconman.2017.03.029.

[21] C. Ortiz, J.M. Valverde, R. Chacartegui, L.A. Perez-Maqueda, P. Giménez, The Calcium-Looping ($CaCO_3$/CaO) process for thermochemical energy storage in Concentrating Solar Power plants, Renew. Sustain. Energy Rev. 113 (2019) 109252, https://doi.org/10.1016/j.rser.2019.109252.

[22] Solar Calcium Looping Integration for Thermochemical Energy Storage (SOCRATCES). Horizon 2020 project. The EU Framework Programme for Research and Innovation, ref.3228/0666https://cordis.europa.eu/project/rcn/212577/factsheet/en., n.d.

[23] J. Blamey, N.P.M. Paterson, D.R. Dugwell, P.S. Fennell, Mechanism of particle breakage during reactivation of CaO-based sorbents for CO_2 capture, Energy Fuels 24 (8) (2010) 4605–4616, https://doi.org/10.1021/ef100476d.

[24] D.P. Hanak, E.J. Anthony, V. Manovic, A review of developments in pilot-plant testing and modelling of calcium looping process for CO_2 capture from power generation systems, Energy Environ. Sci. 8 (8) (2015) 2199–2249, https://doi.org/10.1039/C5EE01228G.

[25] B. Sarrión, A. Perejón, P.E. Sánchez-Jiménez, N. Amghar, R. Chacartegui, J. Manuel Valverde, L.A. Pérez-Maqueda, Calcination under low CO_2 pressure enhances the calcium Looping performance of limestone for thermochemical energy storage, Chem. Eng. J. 417 (2021) 127922, https://doi.org/10.1016/j.cej.2020.127922.

[26] R. Ball, Using the second law first: improving the thermodynamic efficiency of carbon dioxide separation from gas streams in an Endex calcium looping system, Appl. Therm. Eng. 74 (2015) 194–201, https://doi.org/10.1016/j.applthermaleng.2014.02.013.

[27] S. Medina-Carrasco, J.M. Valverde, In situ XRD analysis of dolomite calcination under CO_2 in a humid environment, CrystEngComm. 22 (39) (2020) 6502–6516, https://doi.org/10.1039/D0CE00974A.

[28] B. Sarrion, J.M. Valverde, A. Perejon, L. Perez-Maqueda, P.E. Sanchez-Jimenez, On the multicycle activity of natural limestone/dolomite for thermochemical energy storage of concentrated solar power, Energy Technol. 4 (8) (2016) 1013–1019, https://doi.org/10.1002/ente.201600068.

[29] J.M. Valverde, S. Medina, Reduction of calcination temperature in the calcium looping process for CO_2 capture by using helium. In situ XRD analysis, ACS Sustain Chem. Eng. 4 (12) (2016) 7090–7097, https://doi.org/10.1021/acssuschemeng.6b01966.

[30] B.R. Stanmore, P. Gilot, Review-calcination and carbonation of limestone during thermal cycling for CO_2 sequestration, Fuel Process. Technol. 86 (16) (2005) 1707–1743, https://doi.org/10.1016/j.fuproc.2005.01.023.

[31] R.H. Borgwardt, Calcium oxide sintering in atmospheres containing water and carbon dioxide, Ind. Eng. Chem. Res. 28 (4) (1989) 493–500, https://doi.org/10.1021/ie00088a019.

[32] P.J. Anderson, R.F. Horlock, R.G. Avery, Some effects of water vapor during the preparation and calcination of oxide powders, Proc. Br. Ceram. Soc. 33–42 (1965).

[33] J. Agnew, E. Hampartsoumian, J.M. Jones, W. Nimmo, Simultaneous calcination and sintering of calcium based sorbents under a combustion atmosphere, Fuel. 79 (2000) 1515–1523, https://doi.org/10.1016/S0016-2361(99)00287-2.

[34] V. Fierro, J. Adánez, F. García-Labiano, Effect of pore geometry on the sintering of Ca-based sorbents during calcination at high temperatures, Fuel 83 (13) (2004) 1733–1742, https://doi.org/10.1016/j.fuel.2004.03.011.

[35] R. Barker, The reversibility of the reaction $CaCO_3 \rightleftarrows CaO+CO_2$, J. Appl. Chem. Biotechnol. 23 (10) (1973) 733–742, https://doi.org/10.1002/jctb.5020231005.

[36] K. Kuramoto, S. Fujimoto, A. Morita, S. Shibano, Y. Suzuki, H. Hatano, L. Shi-Ying, M. Harada, T. Takarada, Repetitive carbonation-calcination reactions of Ca-based sorbents for efficient CO_2 sorption at elevated temperatures and pressures, Ind. Eng. Chem. Res. 42 (5) (2003) 975–981, https://doi.org/10.1021/ie0207111.

[37] R. Besson, L. Favergeon, Atomic-scale study of calcite nucleation in calcium oxide, J. Phys. Chem. C. 117 (17) (2013) 8813–8821, https://doi.org/10.1021/jp4002252.

[38] R. Besson, M. Rocha Vargas, L. Favergeon, CO_2 adsorption on calcium oxide: An atomic-scale simulation study, Surf. Sci. 606 (3-4) (2012) 490–495, https://doi.org/10.1016/j.susc.2011.11.016.

[39] D.T. Beruto, A.W. Searcy, M.G. Kim, Microstructure, kinetic, structure, thermodynamic analysis for calcite decomposition: Free-surface and powder bed experiments, Thermochim. Acta 424 (1-2) (2004) 99–109, https://doi.org/10.1016/j.tca.2004.05.027.

[40] C. Rodriguez-Navarro, E. Ruiz-Agudo, A. Luque, A.B. Rodriguez-Navarro, M. Ortega-Huertas, Thermal decomposition of calcite: mechanisms of formation and textural evolution of CaO nanocrystals, Am. Mineral. 94 (4) (2009) 578–593, https://doi.org/10.2138/am.2009.3021.

[41] D. Dollimore, J.G. Dunn, Y.F. Lee, B.M. Penrod, The decrepitation of dolomite and limestone, Thermochim. Acta. 237 (1) (1994) 125–131, https://doi.org/10.1016/0040-6031(94)85191-3.

[42] R.A. McCauley, L.A. Johnson, Decrepitation and thermal decomposition of dolomite, Thermochim. Acta 185 (2) (1991) 271–282, https://doi.org/10.1016/0040-6031(91)80049-O.

[43] J.M. Valverde, S. Medina, Crystallographic transformation of limestone during calcination under CO_2, Phys. Chem. Chem. Phys. 17 (34) (2015) 21912–21926, https://doi.org/10.1039/C5CP02715B.

[44] A.X.S. Bruker, TOPAS 6 User manual, Bruker, 2017.

[45] H.M. Rietveld, A profile refinement method for nuclear and magnetic structures, J. Appl. Crystallogr. 2 (1969) 65–71, https://doi.org/10.1107/S0021889869006558.

[46] R.A. Young, The Rietveld Method, By RA Young, Oxford Univ. Press, Oxford, 1993, p. 312.

[47] A. Le Bail, H. Duroy, J.L. Fourquet, Ab-initio structure determination of LiSbWO6 by X-ray powder diffraction, Mater. Res. Bull. 23 (3) (1988) 447–452, https://doi.org/10.1016/0025-5408(88)90019-0.
[48] Armel Le Bail, Whole powder pattern decomposition methods and applications: a retrospection, Powder Diffr. 20 (4) (2005) 316–326, https://doi.org/10.1154/1.2135315.
[49] J.M. Valverde, A. Perejon, S. Medina, L.A. Perez-Maqueda, Thermal decomposition of dolomite under CO_2: insights from TGA and in situ XRD analysis, Phys. Chem. Chem. Phys. 17 (44) (2015) 30162–30176, https://doi.org/10.1039/C5CP05596B.
[50] R. Otsuka, Recent studies on the decomposition of the dolomite group by thermal analysis, Thermochim. Acta 100 (1) (1986) 69–80, https://doi.org/10.1016/0040-6031(86)87051-4.
[51] H.G. Wiedemann, G. Bayer, Note on the thermal decomposition of dolomite, Thermochim. Acta 121 (1987) 479–485, https://doi.org/10.1016/0040-6031(87)80195-8.
[52] J.M. Valverde, P.E. Sanchez-Jimenez, L.A. Perez-Maqueda, Limestone calcination nearby equilibrium: kinetics, CaO crystal structure, sintering and reactivity, J. Phys. Chem. C. 119 (4) (2015) 1623–1641, https://doi.org/10.1021/jp508745u.
[53] M. Samtani, E. Skrzypczak-Janktun, D. Dollimore, K. Alexander, Thermal analysis of ground dolomite, confirmation of results using an X-ray powder diffraction methodology, Thermochim. Acta. 367–368 (2001) 297–309, https://doi.org/10.1016/S0040-6031(00)00663-8.
[54] P.E. Sánchez-Jiménez, J.M. Valverde, A. Perejón, A. de la Calle, S. Medina, L. A. Pérez-Maqueda, Influence of ball milling on CaO crystal growth during limestone and dolomite calcination: effect on CO_2 capture at calcium looping conditions, Cryst. Growth Des. 16 (12) (2016) 7025–7036, https://doi.org/10.1021/acs.cgd.6b01228.
[55] A.I. Lysikov, A.N. Salanov, A.G. Okunev, Change of CO_2 carrying capacity of CaO in isothermal recarbonation-decomposition cycles, Ind. Eng. Chem. Res. 46 (13) (2007) 4633–4638, https://doi.org/10.1021/ie0702328.
[56] A. Perejón, L.M. Romeo, Y. Lara, P. Lisbona, A. Martínez, J.M. Valverde, The Calcium-Looping technology for CO_2 capture: on the important roles of energy integration and sorbent behavior, Appl. Energy 162 (2016) 787–807, https://doi.org/10.1016/j.apenergy.2015.10.121.
[57] J. Arcenegui-Troya, P.E. Sánchez-Jiménez, A. Perejón, V. Moreno, J.M. Valverde, L.A. Pérez-Maqueda, Kinetics and cyclability of limestone ($CaCO_3$) in presence of steam during calcination in the CaL scheme for thermochemical energy storage, Chem. Eng. J. 417 (2021) 129194, https://doi.org/10.1016/j.cej.2021.129194.
[58] Y. Xu, C. Luo, Y. Zheng, H. Ding, Q. Wang, Q. Shen, X. Li, L. Zhang, Characteristics and performance of CaO-based high temperature CO_2 sorbents derived from a sol-gel process with different supports, RSC Adv. 6 (83) (2016) 79285–79296, https://doi.org/10.1039/C6RA15785H.
[59] J.M. Valverde, P.E. Sanchez-Jimenez, L.A. Perez-Maqueda, Effect of heat pretreatment/recarbonation in the Ca-looping process at realistic calcination conditions, Energy Fuels 28 (6) (2014) 4062–4067, https://doi.org/10.1021/ef5007325.
[60] J.M. Valverde, P.E. Sanchez-Jimenez, L.A. Perez-Maqueda, High and stable CO_2 capture capacity of natural limestone at Ca-looping conditions by heat pretreatment and recarbonation synergy, Fuel (2014), https://doi.org/10.1016/j.fuel.2014.01.045.
[61] A. de la Calle Martos, J.M. Valverde, P.E. Sanchez-Jimenez, A. Perejón, C. García-Garrido, L.A. Perez-Maqueda, Effect of dolomite decomposition under CO_2 on its multicycle CO_2 capture behaviour under calcium looping conditions, Phys. Chem. Chem. Phys. 18 (24) (2016) 16325–16336, https://doi.org/10.1039/C6CP01149G.
[62] J. Blamey, E.J. Anthony, J. Wang, P.S. Fennell, The calcium looping cycle for large-scale CO_2 capture, Prog. Energy Combust. Sci. 36 (2) (2010) 260–279, https://doi.org/10.1016/j.pecs.2009.10.001.
[63] A. March, Mathematische theorie der regelung nach korngestalt bei affiner deformation, Z Krist. 81 (1932) 285–297.
[64] W.A. Dollase, Correction of intensities for preferred orientation in powder diffractometry: application of the March model, J. Appl. Crystallogr. 19 (1986) 267–272. https://doi.org/10.1107/S0021889886089458.
[65] E. Zolotoyabko, Determination of the degree of preferred orientation within the March-Dollase approach, J. Appl. Crystallogr. 42 (3) (2009) 513–518, https://doi.org/10.1107/S0021889809013727.
[66] D. Alvarez, J.C. Abanades, Determination of the critical product layer thickness in the reaction of CaO with CO_2, Ind. Eng. Chem. Res. 44 (15) (2005) 5608–5615, https://doi.org/10.1021/ie050305s.
[67] G. Grasa, R. Murillo, M. Alonso, J.C. Abanades, Application of the random pore model to the carbonation cyclic reaction, AIChE J. 55 (5) (2009) 1246–1255, https://doi.org/10.1002/aic.v55:510.1002/aic.11746.
[68] H. Sun, J. Wang, X. Liu, B. Shen, C.M.A. Parlett, G.O. Adwek, E. John Anthony, P. T. Williams, C. Wu, Fundamental studies of carbon capture using CaO-based materials, J. Mater. Chem. A. 7 (16) (2019) 9977–9987, https://doi.org/10.1039/C8TA10472G.